# A DESIGN METHOD FOR MAGNETIC SUSPENSION AND VIBRATION CONTROL OF LEVITATED BEAMS FOR NONCONTACT PROCESSING

Ming-chih Weng, David L. Trumper
Department of Mechanical Engineering
Massachusetts Institute of Technology
Cambridge, MA 02139, USA

## SUMMARY

This paper presents an integrated approach to magnetic suspension of flexible beams for non-contact processing. The challenges of designing such systems are mainly due to the lightly-damped vibration modes of the suspended structures. Our design goal is to make the suspension robustly stable for beams with varying boundary conditions. In this paper, we propose general design procedures for systems with different dimensions and properties, including structural modelling, sensor design, actuator design, sensor/actuator positioning, and controller design. We demonstrate our proposed ideas in a scaled-down experiment, in which we successfully suspend a 3 m long, 6.35 mm diameter steel tube with varying boundary conditions by using 8 sensors and 8 actuators.

## INTRODUCTION

Many industrial operations center on processing of elongated translating elements, such as steel rolling, plastic film production, paper production, coating, and painting. Noncontact handling of the elements can be advantageous for these existing processes [1] [2] [3], and may serve as the underpinnings for new classes of manufacturing methods. Figure 1 shows an idea developed by Dr. Conrad Smith [4] with the assistance of the second author for the production of painted metal handles for brooms and mops. The challenges of designing such magnetic suspension stages are mainly due to the lightly-damped vibration modes of suspended structures.

In this paper, we focus on the magnetic suspension of ferromagnetic beams for non-contact processing. Our goal is to design a new control system to robustly suspend the object with varying boundary conditions. In the following sections, we develop a generalized method to design such systems, including structural modelling and uncertainty envelope, sensor design, actuator design, sensor/actuator averaging positioning method, and controller design.

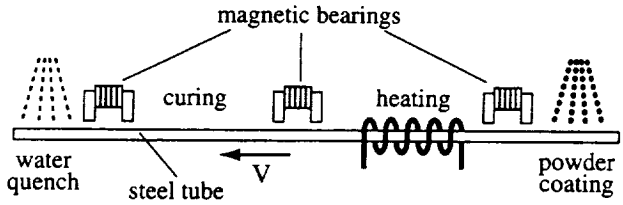


Figure 1: Non-contact coating process

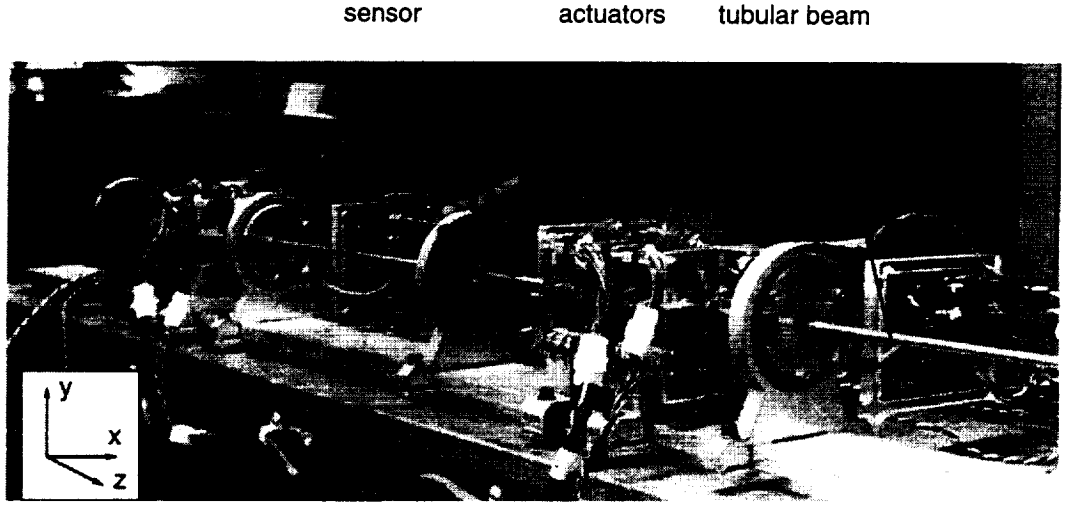


Figure 2: Experimental setup for beam suspension

We demonstrate our proposed ideas in a scaled-down experiment in our lab as shown in Figure 2. We use 8 position sensors and 8 electromagnet actuators to suspend a 3 m long, 6.35 mm diameter steel tube. The experimental results show that the suspended beam is robustly stable under varying boundary conditions, including free, hinged, and clamped boundaries.

## DESIGN REQUIREMENTS AND SYSTEM PROPERTIES

To start designing the system, we first specify the design requirements and system properties. Based on this information, we can then model the system, and design/scale the parameters for sensors, actuators, sensor/actuator positioning, and controllers.

1. Design requirement: sufficient suspension dc stiffness $K$, closed-loop bandwidth $\omega_{BW}$, phase margin within bandwidth $\phi_{PM}$, and airgap $g$.
2. Robustness requirement: varying boundary types (free, hinged, or clamped) and varying boundary positions.

3. Beam properties: bending stiffness $EI$, material density $\rho$, cross-sectional area $A$, axial tension $T$, total length $L$, wall thickness $W$, axial moving velocity $V$, modal damping ratio $\zeta$, electric conductivity $\sigma$, magnetic permeability $\mu$, and magnetic saturation flux density $(B_{sat})_{steel}$.

4. Sensor properties: low-pass dynamics $H_s(s)$, and nonlinear position to voltage relationship.

5. Actuator properties: force function of input current and air gap $F(i, g)$, low-pass dynamics $H_a(s)$, maximum current $i_{max}$ due to limited heat dissipation, and magnetic saturation flux density $(B_{sat})_{lamination}$.

6. Controller speed: calculation time $t_c$ and sampling time $t_s$ for digital control. (time delay $\approx t_c + 0.5t_s$)

## BEAM DYNAMICS AND UNCERTAINTY ENVELOPE

To design the control system, we first model the structural dynamics of beams. We will analyze the beam dynamics by modal analysis, and further derive the uncertainty envelope for varying boundary conditions. Assuming constant bending stiffness $EI$, constant axial tension force $T$, and axial velocity $V$, the dynamic equation of a slender beam can be modelled as a Euler-Bernoulli Beam [5]

$$EI\frac{\partial^4 u}{\partial z^4} - T\frac{\partial^2 u}{\partial z^2} + \rho A\frac{\partial^2 u}{\partial t^2} + 2\rho A\frac{\partial^2 u}{\partial z \partial t}V + \rho A\frac{\partial^2 u}{\partial z^2}V^2 = f, \tag{1}$$

where $z$ is axial coordinate, $u$ is transverse deflection, $\rho$ is material density, $A$ is cross-sectional area, and $f$ is transverse force density. In this paper, we neglect the axial moving velocity $V$ and axial tension force $T$, and thus obtain the simplified beam equation

$$EI\frac{\partial^4 u}{\partial z^4} + \rho A\frac{\partial^2 u}{\partial t^2} = f. \tag{2}$$

The resulting beam dispersion equation

$$EI\lambda^4 = \rho A\omega^2 \tag{3}$$

shows the relation between wavenumber $\lambda$ and frequency $\omega$ for beams. By modal analysis, the beam equation can be decoupled, and the solution can be represented by the superposition of an infinite number of orthogonal modal shapes

$$u(z,t) = \sum_{n=1}^{\infty} \eta_n(t)\phi_n(z), \tag{4}$$

where $\eta_n$ is modal coordinate, and $\phi_n(z)$ is the $n$-th modal shape

$$\phi_n(z) = C_{n1}\cos\lambda_n z + C_{n2}\sin\lambda_n z + C_{n3}\cosh\lambda_n z + C_{n4}\sinh\lambda_n z. \tag{5}$$

The frequency response of the $n$-th mode can be represented as

$$\frac{\eta_n(s)}{N_n(s)} = \frac{1}{M_n(s^2 + 2\zeta_n\omega_n s + \omega_n^2)}, \tag{6}$$

where $N_n$ is the modal force, $M_n$ is the modal mass, $\zeta_n$ is the modal damping ratio, and $\omega_n$ is the mode natural frequency. The first two terms above are defined as

$$N_n(t) = \int_0^L f(z,t)\phi_n(z)dz, \tag{7}$$

$$M_n = \int_0^L \rho A\phi_n^2(z)dz. \tag{8}$$

Combining Equations 4, 6 and 7, if we have a point force input $F$ at $z_a$ and position feedback $y$ at $z_s$, the frequency response from input $F$ to output $y$ can be derived as

$$G(s) = \frac{y(s)}{F(s)} = \sum_{n=1}^{\infty} \frac{\phi_n(z_s)\phi_n(z_a)}{M_n(s^2 + 2\zeta_n\omega_n s + \omega_n^2)}. \tag{9}$$

This shows that the modal shape at sensor $\phi_n(z_s)$ determines the modal observability , and the modal shape at actuator $\phi_n(z_a)$ determines the modal controllability.

To include uncertainty into our beam model, we look at the envelope of the resonance peaks. For a lightly-damped system, the resonance peaks can be approximated by

$$G(j\omega_r) \approx \frac{\phi_r(z_a)\phi_r(z_s)}{2M_r\zeta_r\omega_r^2}. \tag{10}$$

Assuming a normalized sinusoidal modal shape , modal mass $M_r$ can be calculated as

$$M_r = \int_0^L \rho A\phi_r^2 dz = \rho A\int_0^L sin^2(\frac{x}{L}n\pi)dz = \frac{1}{2}\rho AL = \frac{1}{2}m, \tag{11}$$

where $m$ is the total mass of the beam. Assuming the worst case that both $\phi_r(z_a)$ and $\phi_r(z_s)$ are 1, the resonance peak envelope can then be obtained by

$$\boxed{G_{envelope}(\omega) = \frac{1}{m\zeta\omega^2}}. \tag{12}$$

Figure 3 shows the derived peak envelope and the frequency response of a free-free beam model and a hinged-free beam model. Both models assume modal damping ratio $\zeta = 0.005$. This result shows that the peak envelope covers the uncertainty for beams with varying boundary conditions.

We will use the peak envelope in our controller design to include the uncertainty of varying boundary conditions. An important result from Equation 12 is that the designed suspension stiffness will be mainly limited by the beam's total mass $m$ and damping ratio $\zeta$.

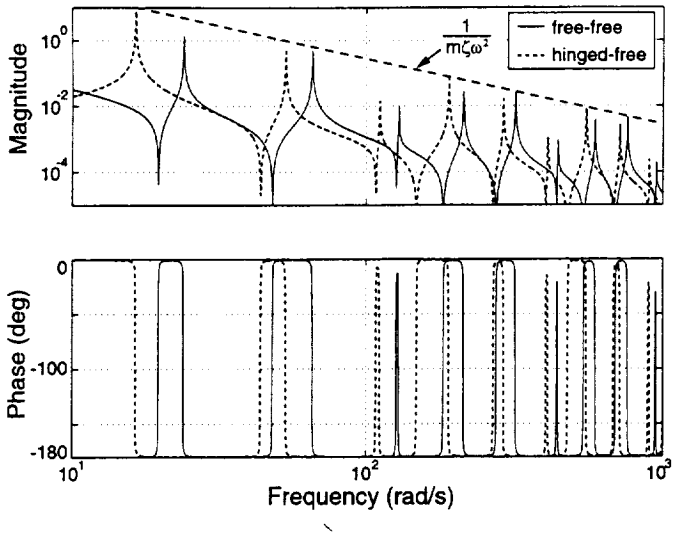


Figure 3: Bode plots of beam models, from force input $F(s)$ to position output $y(s)$: free-free boundaries, hinged-free boundaries, and uncertainty envelope

## SENSOR DESIGN

We have designed a two-dimensional position sensor for the suspension of tubular beams in the form of a two-dimensional variable differential transformer. The reason for choosing this operating principle is that it is robust with respect to surface coatings and dusty environments. The schematic design is shown in Figure 4, the details can be found in [6]. The three primary coils on the poles generate a 6 kHz rotating magnetic field. The

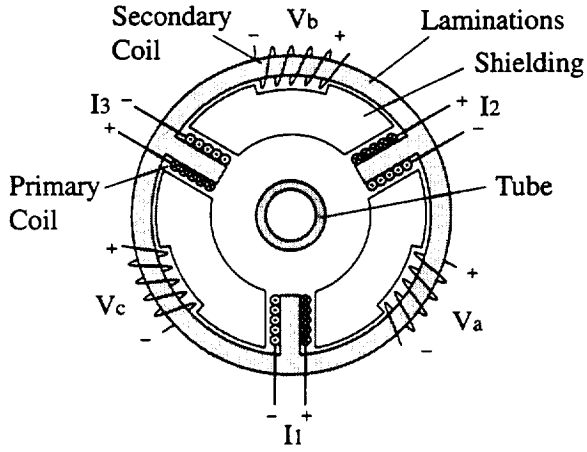


Figure 4: Sensor schematic design

three secondary coils are the outputs that read the magnetic flux rate of change. The $x$ and $y$ positions of the tube are obtained by synchronously detecting the output voltages

$V_a$, $V_b$ and $V_c$ as

$$V_x = \sqrt{3}(V_a \text{sgn}(I_3) - V_c \text{sgn}(I_2))H_s(s), \quad (13)$$

$$V_y = (2V_b \text{sgn}(I_1) - V_a \text{sgn}(I_3) - V_c \text{sgn}(I_2))H_s(s). \quad (14)$$

Here $\text{sgn}(u)$ is the signum function equal to $\pm 1$ depending on the sign of $u$ , and $H_s(s)$ is a low-pass filter with 1 kHz bandwidth. We need to make sure that sensor bandwidth well exceeds the control bandwidth, and the phase lag due to $H_s(s)$ within the control bandwidth must be small to avoid causing difficulties in stabilizing the system.

## ACTUATOR DESIGN

In designing the actuators, we want to obtain the force as a function of current and airgap $F(i, g)$. We also need to predict the maximum force, which is usually limited by coil current due to heat dissipation, and by magnetic flux saturation in the core and in the steel target.

We consider an U-shaped electromagnet made of laminations as shown in Figure 5. To

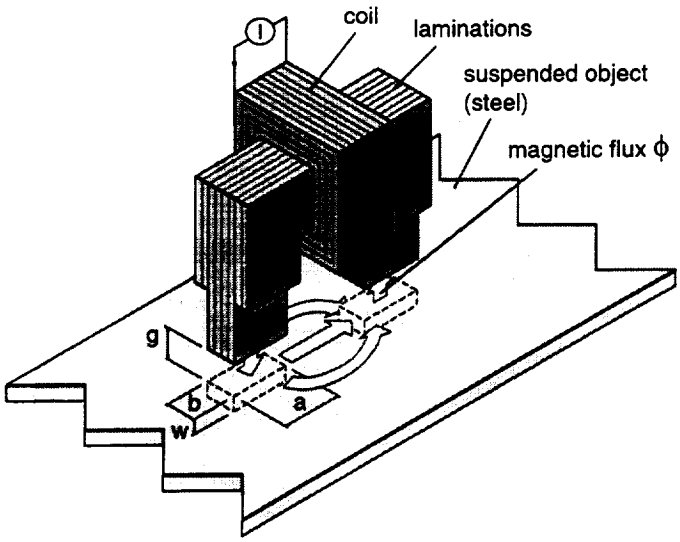


Figure 5: Actuator design

estimate the force function, we neglect fringing field and use a simplified magnetic circuit model. The magnetic flux $B$ and applied force $F$ can be derived as

$$B = \mu_0 \frac{Ni}{2g}, \qquad i < i_{max}, \quad (15)$$

$$F = 2ab\frac{B^2}{2\mu_0} = \frac{\phi^2}{\mu_0 ab}, \qquad \phi < \phi_{max}, \quad (16)$$

where $\mu_0 = 4\pi \times 10^{-7}$ H/m is permeability of air, $N$ is number of turns of coil, $i$ is current input, and $ab$ is cross-sectional area of actuator pole face. A more accurate model can also be derived by solving for the magnetic field distribution analytically or numerically. In our scaled experiment, we predict $F(i,g) = 18i^2/g^2$ from this magnetic circuit model , where $F$ is in Newton, $i$ is in Amp, and $g$ is in mm. In reality we experimentally measure $F(i,g) = 30i^2/g^2$; the difference comes from the neglected fringing field due to the large airgap.

To estimate the maximum force, we first examine the current limit due to heat dissipation in the coil. Air cooled motors usually operate at a thermally-limited current density of about $5 \times 10^6 \text{A/m}^2$ [7]. For example, a 26 gauge wire has $0.13\text{mm}^2$ cross sectional area, and has a current limit of about 0.7 Amp. From the required force, we can decide the wire gauge and turns of coils to use for the actuators.

We further examine the force limit due to magnetic saturation, which can happen inside the actuator or the suspended object. We can follow the magnetic flux loop to find the bottleneck. The saturating flux density $B_{sat}$ is about 1 to 2 Tesla for both Si-Fe laminations and the target steel. For our actuator model, $\phi_{max}$ is limited by $(ab)B_{sat}$ and $(2aW + 2bW)B_{sat}$. We can avoid magnetic saturation by increasing the size of the actuator cores and by increasing the number of actuator poles. In reality, due to the fringing field, the middle part of the actuator core tends to saturate easier than actuator poles.

In this paper, we consider actuators with large air gaps and neglect the eddy currents in the steel target. The reason is that the air reluctance is much larger than material reluctance over the control bandwidth if the airgap is large, hence the magnetic flux is mainly determined by coil current and air reluctance. For actuators with small airgaps, we need to consider the dynamic behavior by including the induced eddy currents at high frequencies, and we will further study it and present the results in a later publication.

## SENSOR/ACTUATOR POSITIONING

One of the greatest problems with the suspension of flexible elements is to maintain stability of high frequency modes. We have developed *sensor interpolation*, *sensor averaging*, and *actuator averaging* methods to address this problem. These methods are derived in [6] and [8]. In fact, our experiment of free-free beam suspension was not stable until we developed the filtering effect of sensor averaging and actuator averaging.

For the sensor interpolation method, we place 2 actuators in between 2 sensors in close proximity, interpolate 2 sensor outputs to estimate the beam deflections at the actuators, in order to reduce sensor/actuator non-collocation problems.

For sensor averaging method, we place 1 actuator at the center between 2 sensors, and average the 2 sensor outputs to estimate the deflection at the actuator. By doing so, we not only eliminate non-collocation problems, we can also adjust the sensor distance to attenuate undesired resonance modes. Assuming a sinusoidal modal shape, with sensors located at $z_1 = (z_0 - d_s)$ and $z_2 = (z_0 + d_s)$, the averaged output is

$$u_{ave}(z_0, t) = \frac{1}{2}(u(z_1, t) + u(z_2, t)) = \sum_{n=1}^{\infty} \eta_n(t)\phi_n(z_0)\underline{\cos(\lambda_n d_s)}. \tag{17}$$

This averaging effect creates a modal band-stop filter of $\cos(\lambda_n d_s)$, which has low gain when $\lambda_n d_s \approx \pi/2$. The cosine effect $\cos(\lambda_n d_s)$, combined with beam dispersion equation $EI\lambda^4 = \rho A\omega^2$, is demonstrated in Figure 6 for the value $d_s = 0.15$ m. The result shows a

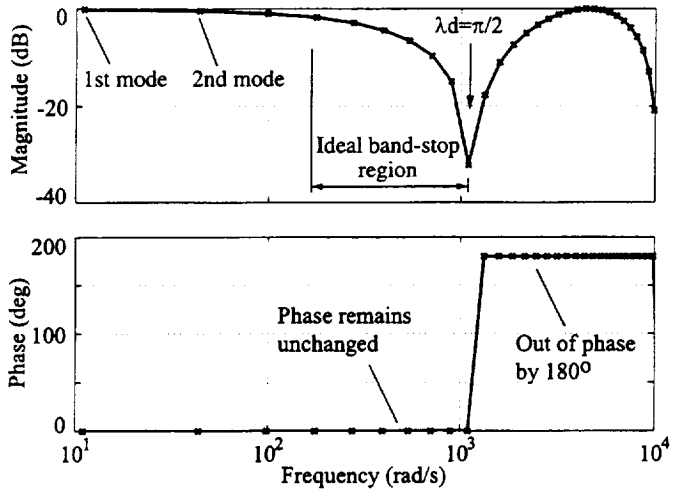


Figure 6: Cosine effect from sensor averaging: a broad notch attenuates several resonance modes, and phase remains unchanged until $\lambda d_s > \pi/2$.

broad notch that attenuates several resonance modes that have wavenumbers near $\pi/2d_s$, and the phase remains unchanged until $\lambda d_s > \pi/2$. Furthermore, this modal filtering effect of $\cos(\lambda_n d_s)$ is a function of beam properties and sensor distance, and is independent of boundary conditions and beam position.

Similarly, for actuator averaging, we place two actuators apart by $2d_a$, and apply the same force on each actuator. We can thereby create another modal band-stop filter of $\cos(\lambda_n d_a)$. Physically the sensor averaging method attenuates the modal observability at the associated frequency range, and actuator averaging method attenuates the modal controllability.

By using this averaging method, we can place the filters near designed cross-over frequency, and hence improve the gain margin without adversely affecting the phase. This averaging effect will be shown in the experiment results in a subsequent section.

## CONTROLLER DESIGN

To deal with the lightly-damped vibration modes of the suspended beam, we design a *slow roll-up lead compensator*, which is a SISO multiple-lead compensator. This compensator has the following structure:

$$H(s) = K_p \frac{(s+m)(s+4m)(s+16m)\cdots}{(s+2m)(s+8m)(s+32m)\cdots}. \tag{18}$$

The controller frequency response is shown in Figure 7. This controller will provide phase margin of about 30 degrees for the frequencies of interest. It has gain rolling up at an average slope of 10 dB/decade to avoid over-amplifying resonance peaks at high frequencies. Depending on the design requirement and structural damping ratio, the ratio of the zero-pole locations can be designed to have more phase margin or slower roll-up rate.

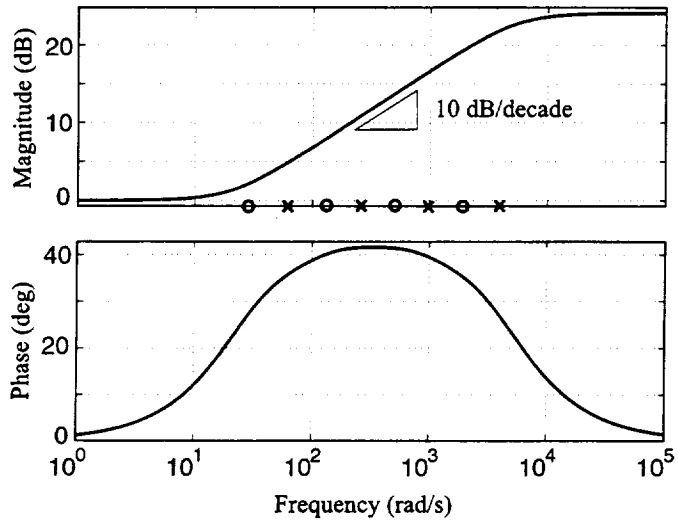


Figure 7: Bode Plots of slow roll-up lead compensator

## SCALED EXPERIMENT

In this section, we describe the design procedures of our beam experiment. Two experimental results are shown. The first experiment uses 2 sensors and 2 actuators to suspend a single point of the beam with clamped-clamped boundaries. The second experiment uses 8 sensors and 8 **actuators** to suspend the beam in 4 units with sensor and actuator averaging within each unit. We also show that the suspension is stable under varying boundary conditions. We first summarize the system properties:

1. Design requirements: suspension dc stiffness $K = 0.4$ N/mm, bandwidth $\omega_{BW} = 100$ Hz, airgap 3 mm, and varying boundary conditions.

2. Beam: $E = 200$ GPa, $I = 58.4$ mm$^4$, $\rho = 7800$ kg/m$^3$, $A = 15$ mm$^2$, $L = 3$ m, , $\zeta = 0.001$, $\sigma = 7.5 \times 10^6$ mhos/m, and $\mu = 5 \times 10^3 \mu_0$ H/m.

3. Sensor: bandwidth of 1 kHz.

4. Actuator: $a = 13$ mm, $b = 3$ mm, $c = 25$ mm, $N = 1200$, 26 gauge wire, current limit $i_{max} = 0.7$ A, and bandwidth 500 Hz.

5. Controller: $t_s = 250\mu$s and $t_c = 220\mu$s. (delay$\approx 345\mu$s)

From the beam properties, we can derive the structure peak envelope. Assuming proportional control of gain $K$, the loop transfer function becomes

$$KG_{envelope}(\omega) = \frac{K}{m\zeta\omega^2} = \frac{2800K}{\omega^2}.\Big( = \frac{K}{140} \text{ at 100 Hz}\Big)\Big( = \frac{K}{400} \text{ at 170 Hz}\Big) \qquad (19)$$

This result shows how the design of control bandwidth and stiffness is constrained to the mass and damping ratio of the beam. It suggests that if we choose dc stiffness $K = 140$ N/m, we will have resonance peaks below 0 dB when frequencies are higher than 100 Hz, and thus we need positive phase margin at least up to 100 Hz. Similarly, if we choose dc stiffness $K = 400$ N/m, we will need positive phase margin up to 170 Hz. From the two design requirements of $\omega_{BW} \geq 100$ Hz and $K \geq 400$ N/m, we choose $K = 400$ N/m to meet both requirements.

Furthermore, we arrange sensor averaging to attenuate the vibration modes around 170 Hz. From the beam dispersion equation, we have

$$EI\lambda^4 = \rho A\omega^2 \Rightarrow \lambda^2 = 0.1\omega \Rightarrow \lambda = 10.3 \text{ at 170 Hz}, \qquad (20)$$

therefore we place 2 sensors apart by $2d_s$ with $d_s = \frac{\pi}{2\lambda} = 0.15$ m.

In our first experiment, we used 2 sensors and 2 actuators to control one point ($z_0 = 1.12$ m) of a clamped-clamped beam. We compared the two positioning methods of sensor interpolation and sensor averaging. In the first arrangement, we placed 2 actuators in between 2 sensors in close proximity and used sensor interpolation method. we were almost able to stabilize the system, except there is a limit cycle vibration at 1100 rad/s. In the second arrangement, we used sensor averaging by placing two sensors at $\pm 0.15$ m from the center, and used the same controller. We were able to stabilize the system and avoid the limit cycle. Figure 8 shows the loop transfer function of both experiments. The loop has 30° phase margin for all vibration modes below 500 rad/s. Below 1000 rad/s, we have an alternating pole-zero pattern, which means each resonance mode is in phase, and hence shows there is no non-collocation problem. Above 1000 rad/s, the modes become

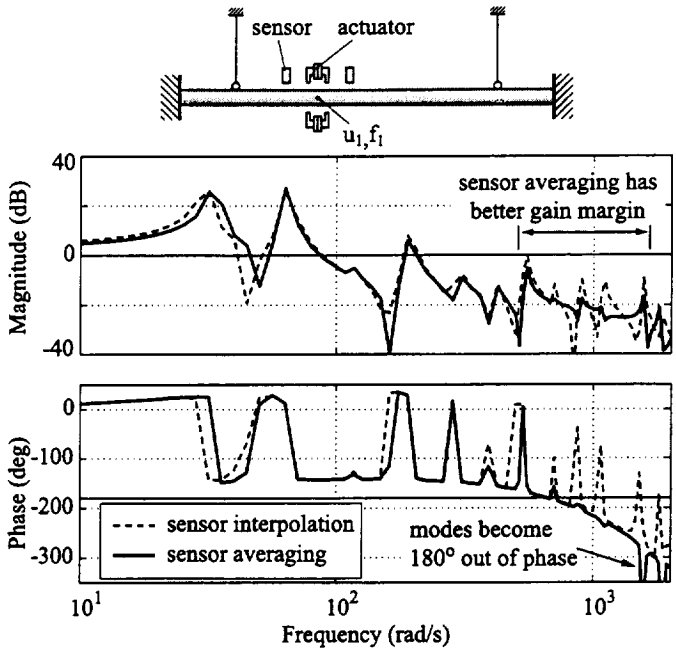


Figure 8: Experimental setup and experimental Bode plots of loop transfer function $H(s)G(s)$, sensor interpolation and sensor averaging

out of phase due to sensor averaging when $\cos(\lambda d_s) < 0$. The sensor averaging shows its advantage around the cross-over frequency, where it attenuates the vibration modes without affecting the phase, and hence improves the stability robustness by increasing the gain margin.

In our second experiment, we used 8 sensors and 8 actuators to control 4 points of the beam with varying boundary conditions. We compared two different arrangements: sensor averaging only, and both sensor/actuator averaging. In the first arrangement, we used the sensor averaging method only, and were able to stabilize the beam with loosely clamped boundaries. However, when the beam was released to free-free boundaries, a vibration at 800 Hz builds up and destabilizes the system in a few seconds. In the second arrangement, we added actuator averaging to the previous sensor averaging arrangement. To attenuate vibration modes around 800 Hz, we placed two actuators apart by $2d_a$ with $d_a = 0.07$ m, and we were able to suspend the beam with varying boundary conditions, including clamped, hinged, and free boundaries. The Bode plots of $H(s)G_{22}(s)$ for a suspended free-free beam is shown in Figure 9, where $G_{22}(s)$ is the open-loop dynamics of the 2nd control point at $z_0 = 1.12$ m. The result shows the damping ratio of the beam is below 0.001. An interesting observation is that the free-mass dynamics of $1/(ms^2)$ is not observed in the Bode plots. That is because the measured horizontal dynamics are coupled to vertical dynamics, and the low frequency dynamics are determined by a pendulum mode with natural frequency of 20 rad/s, which appears as a small bump in Figure 9.

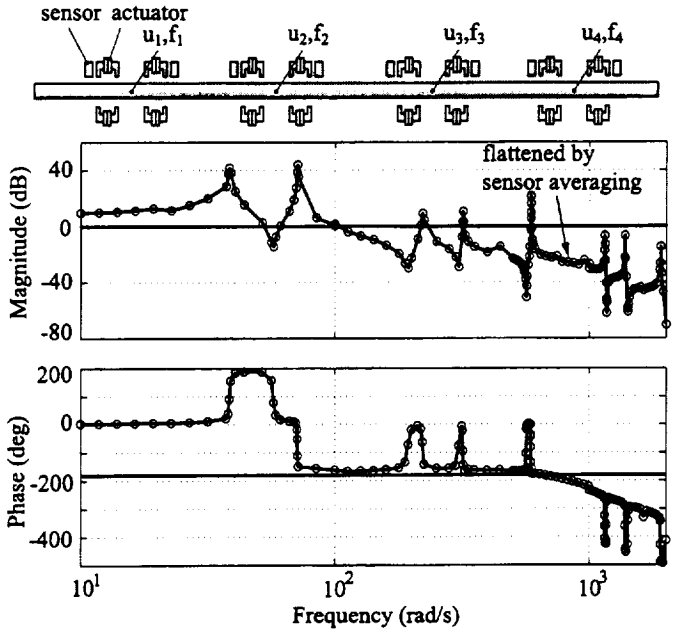


Figure 9: Experimental setup and experimental Bode plots of $H(s)G_{22}(s)$ for free-free beam suspension

## CONCLUSION

This paper presents general design procedures for magnetic suspension of elongated beams for noncontact processing. We derived the uncertainty envelope that represents the beam dynamics with varying boundary conditions, and used it to guide the controller design. We developed sensor and actuator averaging methods to attenuate undesired resonance modes without adversely affecting phase. We also built a scaled experiment to suspend a tubular beam, and demonstrated the effectiveness of our proposed design method. In the future, we plan to further study the effects of beam axial velocity $V$ and axial tension $T$. We will also investigate the dual problem of electrostatic levitation, and the suspension of different structures, including strings, membranes, and plates.

## ACKNOWLEDGMENTS

This research is sponsored by the National Science Foundation under Grant Award Number DMI-9700973. The authors wish to acknowledge Professor Jeffrey H. Lang and Professor Samir Nayfeh at MIT for their helpful comments.

# References


[1] Y. Oshinoya and T. Shimogo "Electro-magnetic Levitation Control of an Elastic Plate," in *Proc. Maglev '89*, pp. 435-440, 1989.

[2] H. Hayasiya, H. Ohsaki, and E. Masada "Magnetic Levitation Control of Elastic Steel Plate for Steel Making Process," in *Proc. ICEE '95*, 1995.

[3] J. Jin, T. C. Yih, T. Higuchi, and J. U. Jeon, "Direct Electrostatic Levitation and Propulsion of Silicon Wafer," *IEEE Trans. Industry Applications*, vol. 34, No. 5, pp. 975-984, 1998.

[4] American Metal Handle, Vulcan Dr., Birmingham, AL, USA.

[5] J. A. Wickert and C. D. Mote, Jr., "Classical Vibration Analysis of Axially Moving Continua," *Journal of Applied Mechanics, Transactions of the ASME*, Vol. 57, pp.738-744, September 1990.

[6] D. L. Trumper, M. C. Weng, and R. J. Ritter, "Magnetic Suspension and Vibration Control of Beams for Non-contact Processing," *Proc. of the 1999 IEEE International Conference on Control Applications*, pp. 551-557, 1999.

[7] M. K. Liebman, "Thermally Efficient Linear Motor Analysis & Design," Chapter 3, Master's Thesis, MIT Dept. of Mechanical Engineering, 1996.

[8] M. C. Weng and D. L. Trumper, "Vibration Control of Flexible Structures Using Sensor Averaging and Actuator Averaging Methods," submitted to the *IEEE Transactions on Control Systems Technology.*